Supporting Information

Perovskite Quantum Dots Encapsulated in Mesoporous Metal–Organic Framework as Synergistic Photocathode Materials

Guan-Yu Qiao,[†,‡] Dehui Guan,[†,‡] Shuai Yuan,[§] Heng Rao,[†,#] Xiao Chen,[¶] Jia-Ao Wang,[+] Jun-Sheng Qin,[†,#,*] Ji-Jing Xu,[†,#,*] and Jihong Yu[†,#,*]

[†]State Key Laboratory of Inorganic Synthesis and Preparative Chemistry, College of Chemistry, Jilin University, Changchun 130012, P. R. China
[§]State Key Laboratory of Coordination Chemistry, School of Chemistry and Chemical Engineering, Collaborative Innovation Center of Advanced Microstructures, Nanjing University, Nanjing 210023, P. R. China
[¶]Beijing Key Laboratory of Green Chemical Reaction Engineering and Technology, Department of Chemical Engineering, Tsinghua University, Beijing 100084, P. R. China.
[+]Department of Chemistry and the Oden Institute for Computational Engineering and Sciences, The University of Texas at Austin, Austin, TX, 78712-0165, USA.
[#]International Center of Future Science, Jilin University, Changchun 130012, P. R. China

[‡]These authors contributed equally.

Correspondence and requests for materials should be addressed to J.-S.Q. (*qin@jlu.edu.cn), J.-J.X. (*jijingxu@jlu.edu.cn) and J.Y. (*jihong@jlu.edu.cn).

Table of Contents

S1. Materials and Instrumentation

Materials

All reagents and solvents were commercially available and used as received, except for H_3TATB. Lead bromide ($PbBr_2$), cesium bromide (CsBr), polyvinylidene difluoride (PVDF), N-methyl-2-pyrrolidone (NMP), tretraethylene glycol dimethyl ether (TEGDME), and lithium bis(trifluoromethanesulphonyl)imide (LiTFSI) were purchased from Aladdin Reagent. Lithium sheets were purchased from China Energy Lithium Co., Ltd. (Tianjin, China). The abbreviation for some solvents and reagents were listed here: 1,2-dimethoxyethane (DME), CH_2Cl_2 (DCM), N,N-dimethylformamide (DMF), N,N-diethylformamide (DEF), dimethylsulfoxide (DMSO), and tetrahydrofuran (THF).

Instrumentation

Synthetic operations that require an inert atmosphere (where noted) were performed under nitrogen using standard Schlenk techniques. TEM, HRTEM, HADDF STEM, and EDS mapping were obtained using a JEOL JEM-2100F microscope coupled with X-Max N 80T EDS detector from Oxford Instruments. The morphologies and structures of samples were characterized by using SEM (JEOL JSM-6700F) equipped with element mapping energy-dispersive spectrometer. Powder X-ray diffraction (PXRD) was collected with a Rigaku D-Max 2550 diffractometer using Cu $K_α$ radiation at a 4° min^{-1} scan rate. XPS measurements were performed on an ESCALAB 250 photoelectron spectrometer. Photoluminescence quenching spectra were collected using the FLUOROMAX-4 spectrophotometer. Room-temperature UV–vis absorption measurements were obtained by a U-4100 UV–vis spectrometer under the diffuse-reflection model using an integrating sphere (UV 2401/2, Shimadzu). N_2 adsorption-desorption isotherms at 77 K were conducted using a Micrometritics ASAP 2020 system. ^1H Nuclear magnetic resonance (NMR) spectra were collected on a Varian 300 MHz NMR spectrometer. The metal loading was determined using inductively coupled plasma (ICP) analyses on a PerkinElmer Optima 3300 DV ICP instrument. The thermogravimetric analysis (TGA) curves of the samples were carried out using a TGA Q500 analyzer heated from room temperature to 800 °C in air with the heating rate of 10 °C·min^{-1}. DEMS was performed on i-DEMS 100.

S2. Syntheses

Synthesis of Ligand
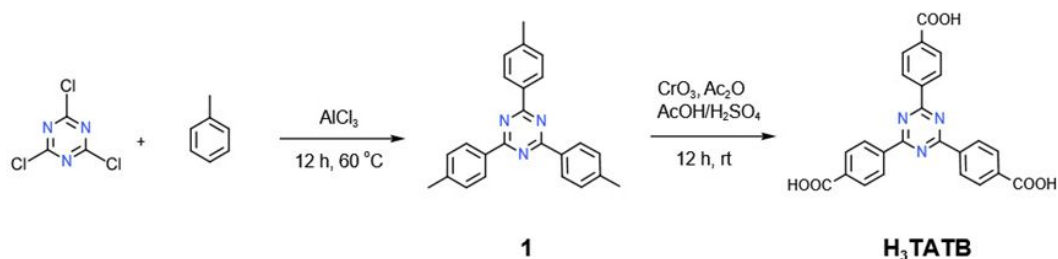
Scheme S1. The synthetic route of H₃TATB.

2,4,6-tri-p-tolyl-1,3,5-triazine (1). To a three-neck flask, AlCl$_3$ (20 g) was dissolved in dry toluene and heated to 60 °C. C$_3$N$_3$Cl$_3$ (8.3 g) was then added portion-wise for an hour and the mixture was stirred overnight. Then resulting red sticky oil was poured into a large amount of ice water to quench the catalyst and extracted with CHCl$_3$. After removing solvent, a crude product was precipitated out from methanol to yield a needle-like solid. Resulting solid was recrystallized from hot toluene to afford a white needle-like crystalline solid (10 g, 63%). ^{1}H NMR (300 MHz, CDCl$_3$): δ = 8.64 (d, 6 H), 7.35 (d, 6 H), 2.46 (s, 9 H).

4,4′,4″-s-triazine-2,4,6-triyl-tribenzoic acid (H₃TATB). To a 500 mL three-necked flask **1** (2.78 g) was dissolved in acetic acid (70 mL) and then 4.4 mL of H$_2$SO$_4$ was added. A solution of chromium oxide (7.2 g) in acetic anhydride (4.8 mL) was carefully added into the reaction flask with an ice bath. The resulting dark-green slurry was stirred overnight. The reaction mixture was poured into 250 mL cold water, stirred 1 h to well mixed, and filtered. The solids were washed with water to remove chromium acid. Dissolve the white solid in 200 mL 2 M NaOH solution. After the unreacted starting material was removed by filtration, the solution was acidified with 6 M HCl solution to give white crude product (until pH < 3). Resulting crude product was then filtered and dried. Recrystallization from DMF afforded pure product as a white solid (3.0 g, 86%). ^{1}H NMR (300 MHz, DMSO-d_6): δ = 13.35 (s, 3 H), 8.85 (d, 6 H), 8.20 (d, 6 H).

Synthesis of PCN-333(Fe)

H$_3$TATB (60 mg) and anhydrous FeCl$_3$ (60 mg) were dissolved in 10 mL DEF, then trifluoroacetic acid (0.6 mL) was added. The mixture was heated in 150 °C

oven for 12 h until brown precipitate formed. The resulting brown precipitate was centrifuged and washed with fresh DMF for several times. Yield (based on ligand): ~ 80%.

Synthesis of CsPbBr$_3$ QDs

In a general synthesis method of CsPbBr$_3$ QDs, PbBr$_2$ (0.2 mmol) and CsBr (0.1 mmol) were dissolved in a DMSO solution (5 mL). DMSO acted as a good solvent to dissolve inorganic salts. After complete dissolution, oleic acid (OA) (100 μL) and oleylamine (OM) (50 μL) were added to stabilize the precursor solution. Then, 0.4 mL of the precursor solution was quickly injected into 5 mL of toluene to induce QD crystallization via vigorous stirring. Bright green emission was observed immediately after the injection.

Synthesis of CsPbBr$_3$@PCN-333(Fe)

As-synthesized PCN-333(Fe) powder (50 mg) immersed in 5 mL of PbBr$_2$ DMSO solution (0.04 M) for 2 h, then used DMSO/ethanol to wash away PbBr$_2$ on the surface of PCN-333(Fe). The obtained PbBr$_2$@PCN-333(Fe) was immersed in 5 mL of CsBr DMSO solution (0.02 M) for 1 h, then oleic acid (OA) (20 μL) and oleylamine (OM) (10 μL) were added to stabilize the precursor solution and toluene was added to generate CsPbBr$_3$ perovskite nanoparticles. The material obtained by centrifugation was washed three times with n-hexane to obtain the final CsPbBr$_3$@PCN-333(Fe) composite.

S3. Photoelectrochemical Measurements

Mott-Schottky measurements were measured in a three-electrode with Li foil as the counter electrode and the reference electrode configuration using a CHI660A electrochemical workstation in 1 M LiTFSI/TEGDME at a scan rate of 50 mV s^{-1}. The linear sweep voltammetry (LSV) was employed in the same three-electrode system with Li foil as the counter electrode and the reference electrode, and O$_2$-saturated 1 M LiTFSI/TEGDME solution with and without irradiation to evaluate the ORR and OER performance, respectively. The quantitative in situ differential electrochemical mass spectrometry (DEMS) was performed to monitor the amounts of O$_2$ consumption and evolution during the ORR and OER processes, respectively.

S4. Photo-assisted Li−O$_2$ Battery Assembly and Electrochemical Measurements

The cathodes slurry was prepared by homogeneously mixing the active material (CsPbBr$_3$@PCN-333(Fe), PCN-333(Fe), and CsPbBr$_3$, respectively, 90 wt%) and PVDF (10 wt%) in NMP solvent. Subsequently, the porous photo-electrode was obtained by spraying the slurry on a carbon paper with a diameter of 12 mm and dried in a vacuum at 60 °C for 12 h to remove the residual solvent. The mass loading is about 0.8 mg cm^{-2}. The photo-assisted Li–O$_2$ battery was performed in an Ar-filled glovebox (O$_2$ < 0.1 ppm; H$_2$O < 0.1 ppm). The cell consists of a Li anode (16 mm), a glass fiber separator, a porous photo-electrode, and a current collector in 1.0 M LiTFSI/TEGDME, simultaneously with a transparent window for light illumination. The as-prepared batteries were tested in home-made bottles filled with pure O$_2$. The discharge/charge curves were obtained with a Land-CT2001A battery-testing system. The round-trip efficiency is calculated according to equation 1:

$$\text{Round - trip efficiency} = \frac{\text{discharge platform}}{\text{charge platform}} \times 100\%$$

(1)

S5. Computational Parameters

All theoretical investigations were performed via the VASP code (Vienna Ab initio Simulation Package).[1] Geometry optimizations were conducted using the highly accurate generalized gradient approximation (GGA) method with the Perdew-Burke-Ernzerhof (PBE) exchange correlation function.[2] The cutoff energy, k-point, and the type of K-mesh were set to 400 eV and Gamma-centered,[3] respectively. And the static calculation was collected based on the electron-step energy convergence criterion and ion-force convergence criterion of 10^{-5} eV. In order to get a better convergence for the appearance of d and f orbital, the LMAXMIX tag was set to 6 in considering of f orbital mixing effect. In addition, to get a good charge density plot, FFT grid mesh density was set to (180, 180, 180), in x, y, z-axis respectively. To speed up the process of convergence, LREAL tag in VASP software was turned on. LWAVE, LCHAEG and ADDGRID tags were both set to .TURE.. The smearing method was Gaussian smearing method, and the width of SIGMA was 0.5 for the edge of Fermi energy smooth. Electronic step convergence standard was set to 1E-08, to get an accurate electronic structure

when plotting the wavefunction projected to real space. The subtraction methodology for the charge density was carefully do the two calculation for one 3-demensional charge density difference. In terms of model building, owing to its huge amount of atoms, the primitive part of PCN-333(Fe) were picked out for DFT calculation. Simple cubic lattice perovskite of $CsPbBr_3$ was directly employed without relaxation in consideration of the simulation of the periodic edge perovskite. Though, this is just a demonstrative charge density difference showing the simple charge transfer situation, which is a simulation of the real PCN-333(Fe) charge exchanging; however, this can only be used to illustrate its confined merits for PCN-333(Fe) to the perovskite of $CsPbBr_3$.

S6. Digital Photos of Materials under Ultraviolet Irradiation
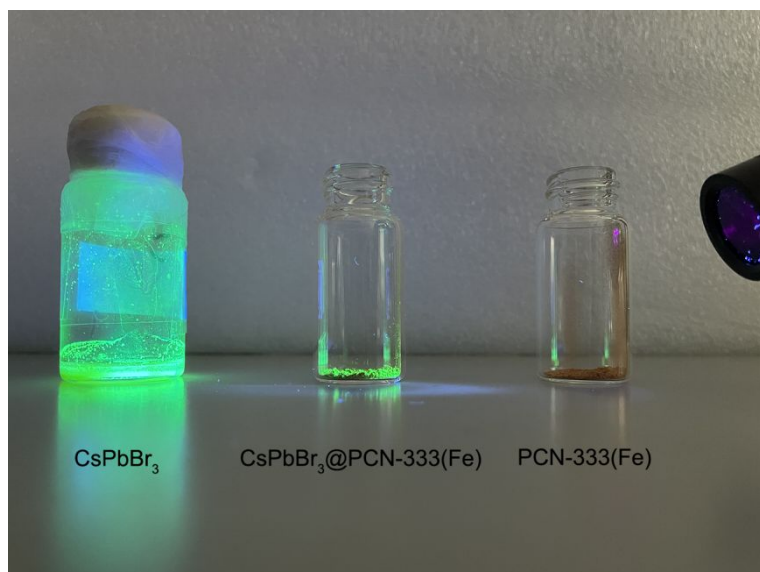
Figure S1. Digital photos of CsPbBr$_3$@PCN-333(Fe), PCN-333(Fe), and CsPbBr$_3$ under ultraviolet irradiation.

S7. PXRD Patterns
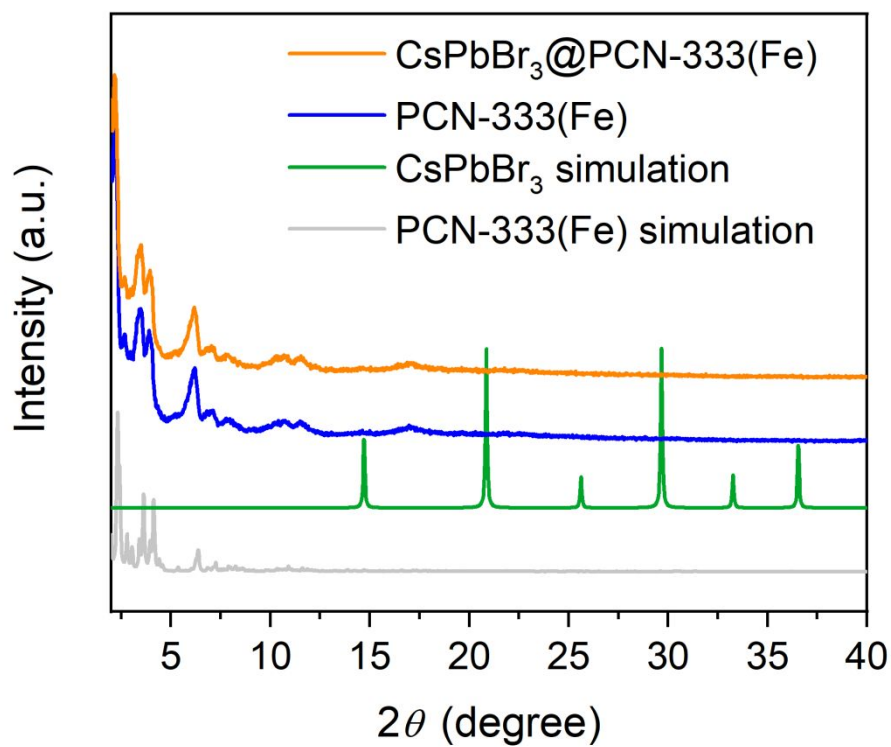
Figure S2. PXRD patterns of simulated and as-synthesized materials.

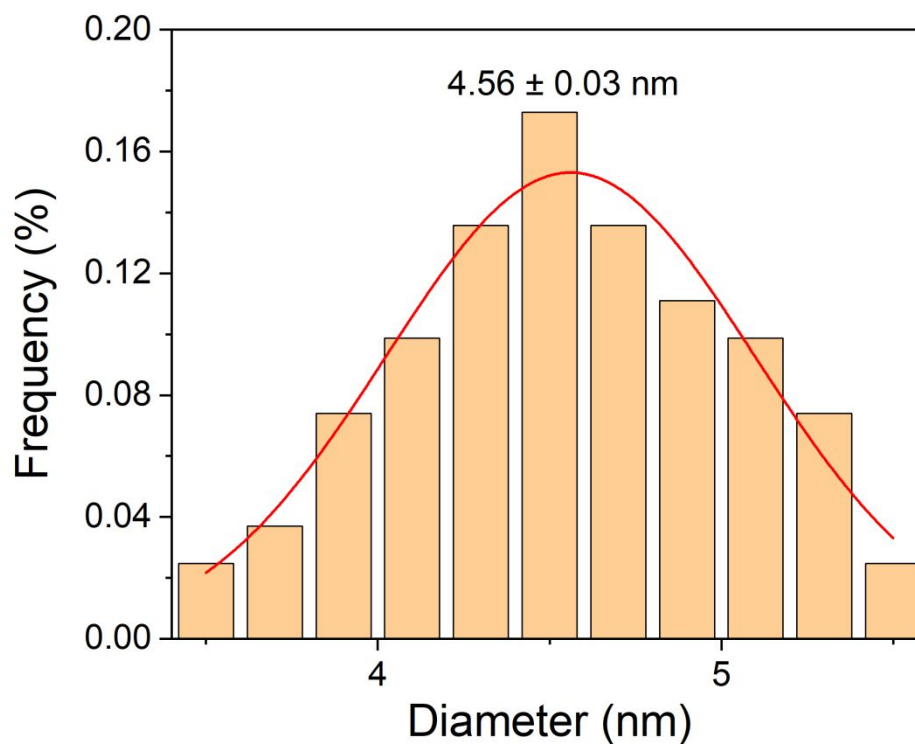**S8. Size Distribution of as-prepared CsPbBr$_3$ QDs in CsPbBr$_3$@PCN-333(Fe)**

Figure S3. Diameter distribution histograms of as-prepared CsPbBr$_3$ QDs in the CsPbBr$_3$@PCN-333(Fe).

The size of CsPbBr$_3$ QDs in the CsPbBr$_3$@PCN-333(Fe) was estimated by ImageJ software and found to almost be in the range of 4–5 nm.

S9. EDS Mapping
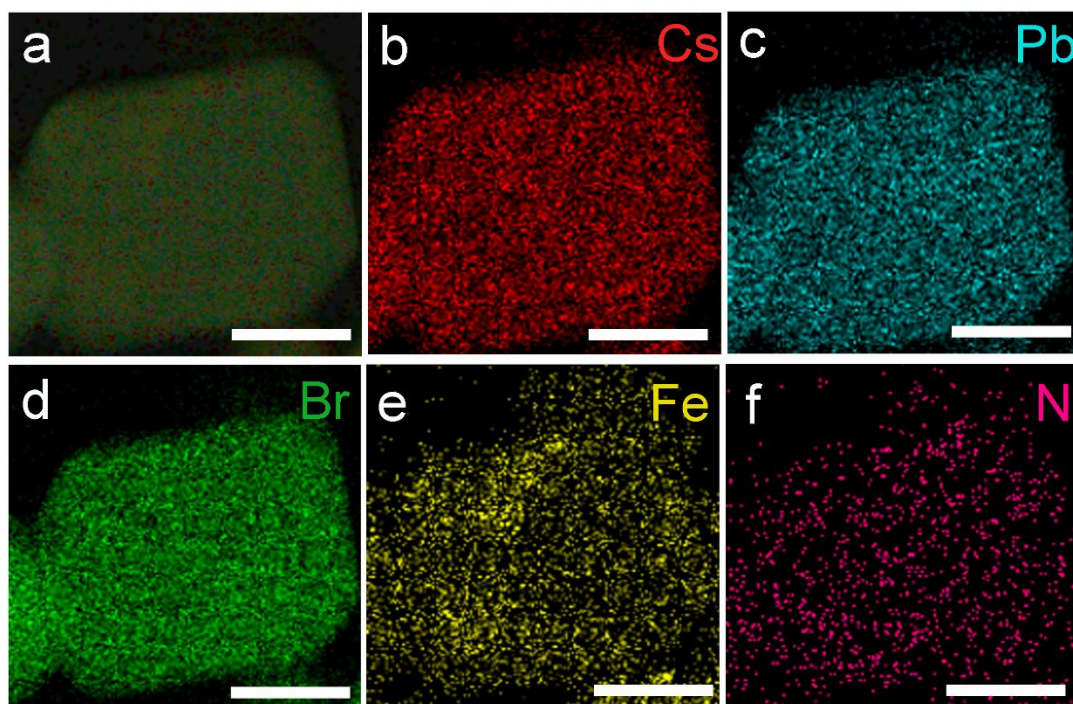
Figure S4. (a-f) EDS mapping for CsPbBr$_3$@PCN-333(Fe). Scale bars: (a-f) 150 nm.

Element	Wt %	AT %
Fe	44.13	31.35
N	19.86	56.35
Cs	5.03	1.6
Pb	14.55	2.8
Br	16.42	7.9
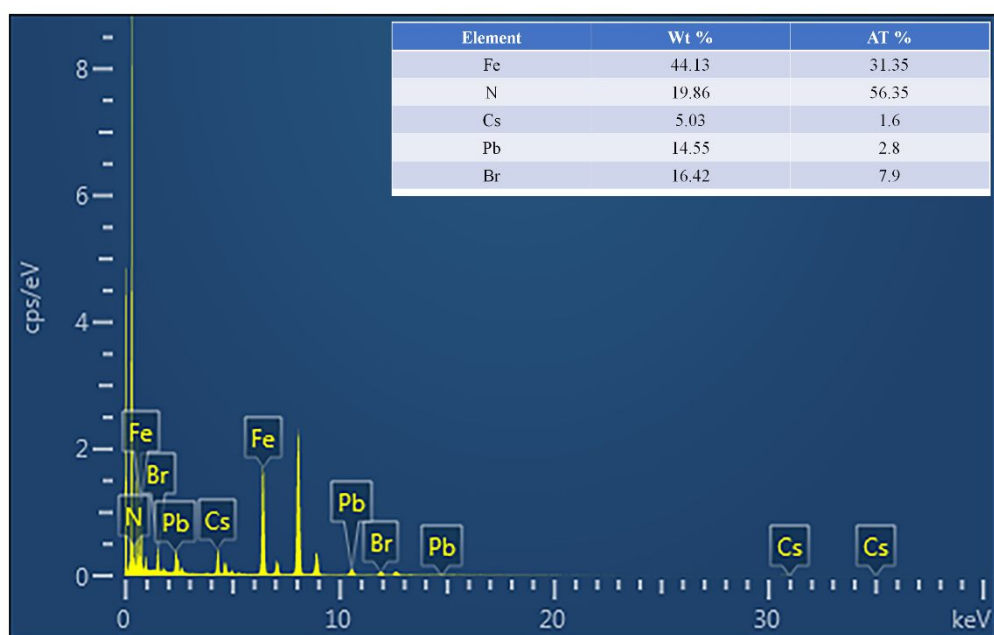
Figure S5. EDS spectrum of CsPbBr$_3$@PCN-333(Fe) with the elemental composition analysis.

The theoretical ratio of Fe: N is 1: 2, and the actual measured value is 1:1.8; the theoretical ratio of Cs: Pb: Br is 1: 1: 3, and the actual measured value is 1: 1.7: 5.

S10. Thermogravimetric Analysis
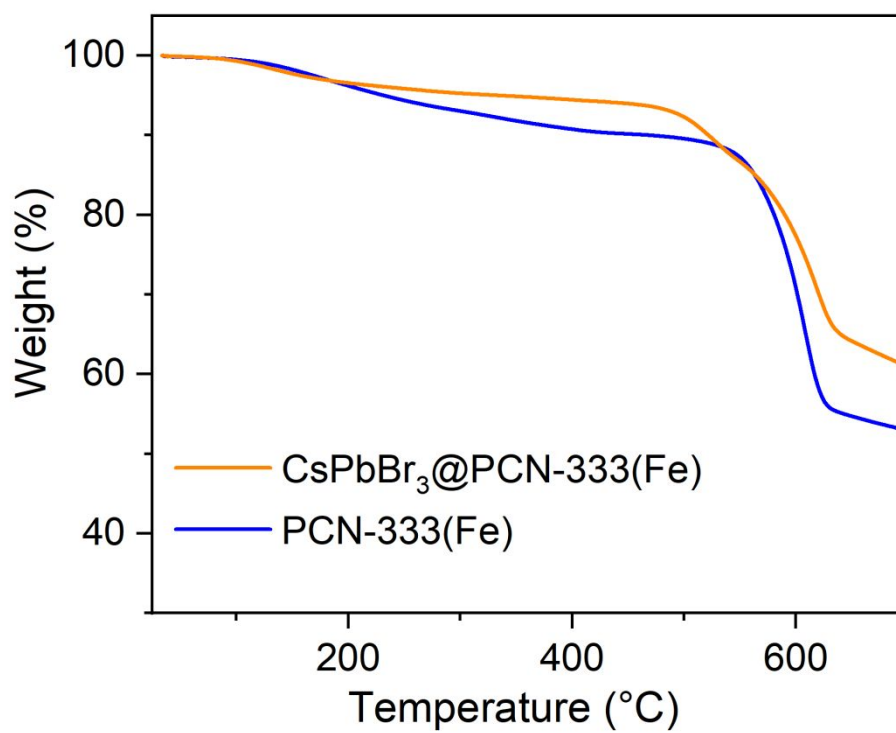
Figure S6. TGA for CsPbBr$_3$@PCN-333(Fe) and PCN-333(Fe).

S11. N$_2$ Sorption Isotherms

Sample activation procedure. Thoroughly washed samples underwent solvent exchange with acetone followed by hexanes at least five times, respectively and dried in a pre-heated 85 °C oven for 30 min. Resulting powder was then activated for BET measurement at 150 °C for 2 h.
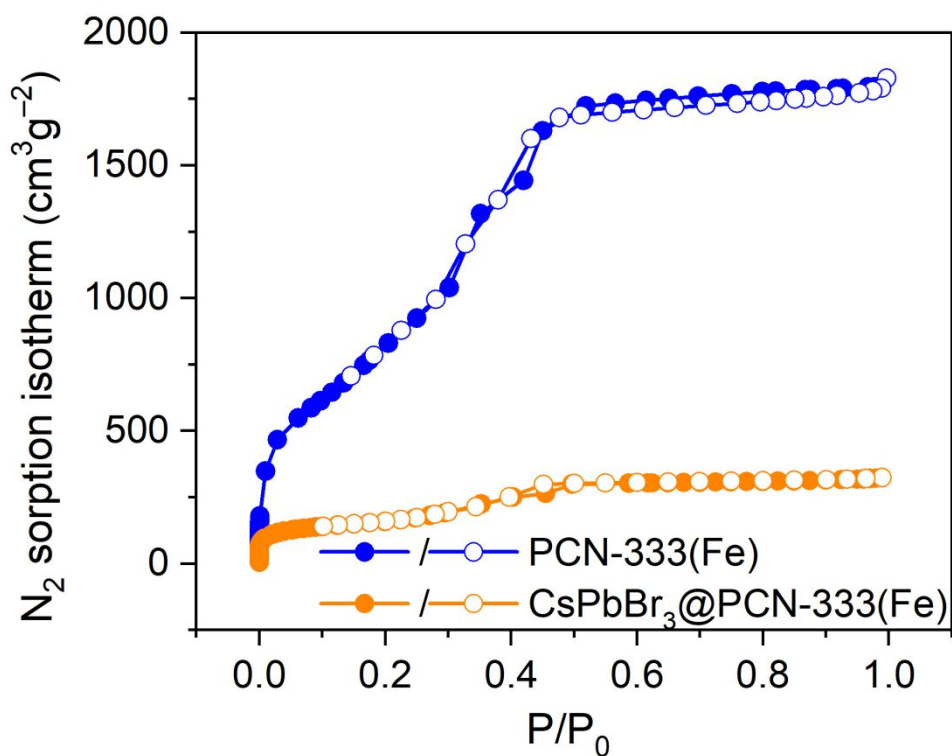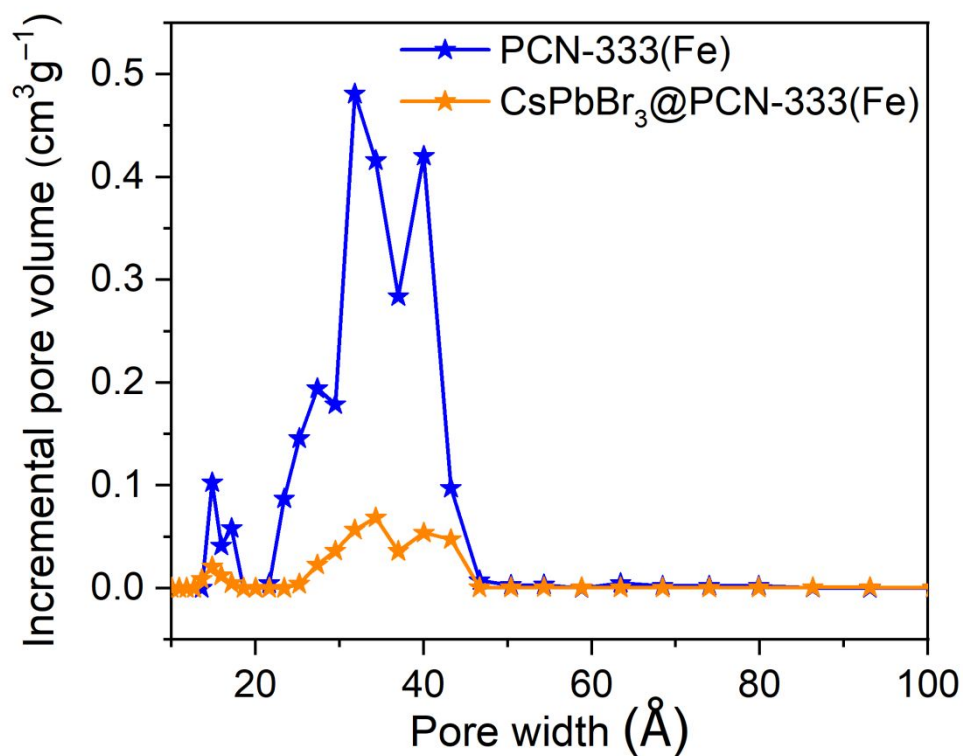

Figure S7. N$_2$ sorption isotherms of PCN-333(Fe) and CsPbBr$_3$@PCN-333(Fe) at 77 K and 1 atm.

S12. Pore Volume and Pore Size Distribution Calculation

Sample activation procedure. Thoroughly washed samples underwent solvent exchange with acetone followed by hexanes at least five times, respectively and dried in a pre-heated 85 °C oven for 30 min. Resulting powder was then activated for BET measurement at 150 °C for 2 h.

Figure S8. Comparison of DFT pore size distributions before and after encapsulating the perovskite (obtained from N_2 sorption isotherm at 77 K and 1 atm).

S13. IR Spectra
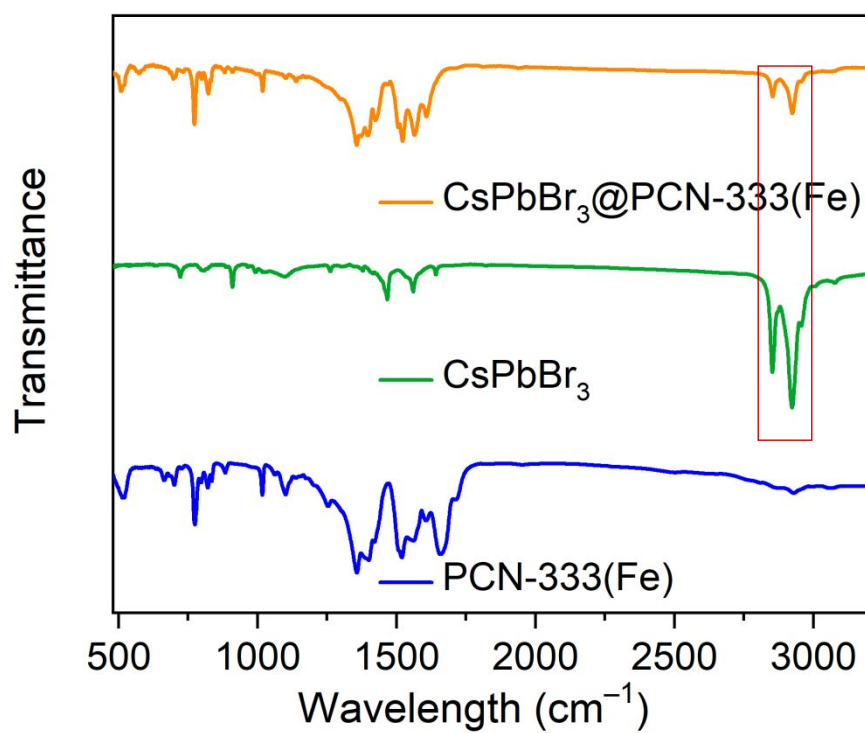
Figure S9. IR spectra of CsPbBr$_3$@PCN-333(Fe), CsPbBr$_3$ and PCN-333(Fe).

S14. X-ray Photoelectron Spectroscopy (XPS) Study
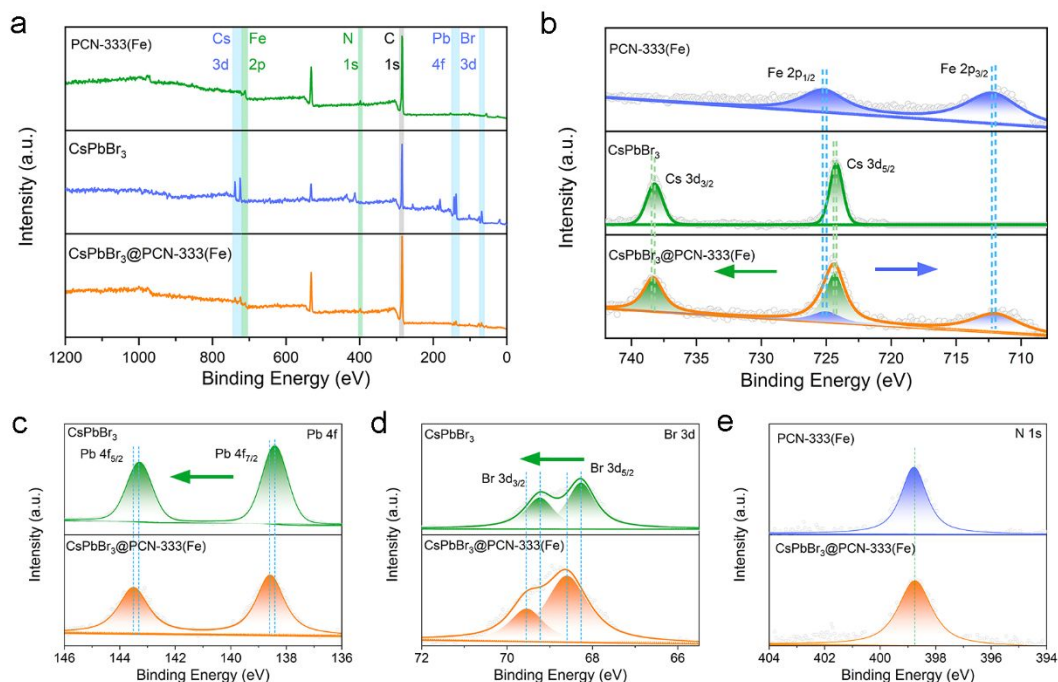
Figure S10. (a) The survey XPS spectra for PCN-333(Fe), CsPbBr$_3$, and CsPbBr$_3$@PCN-333(Fe). (b) High-resolution XPS spectra of Cs 3d and Fe 2p for PCN-333(Fe), CsPbBr$_3$, and CsPbBr$_3$@PCN-333(Fe). (c-d) High-resolution XPS spectra of Pb 4f and Br 3d for CsPbBr$_3$ and CsPbBr$_3$@PCN-333(Fe). (e) High-resolution XPS spectra of N 1s for PCN-333(Fe) and CsPbBr$_3$@PCN-333(Fe).

S15. Model Section Schematic
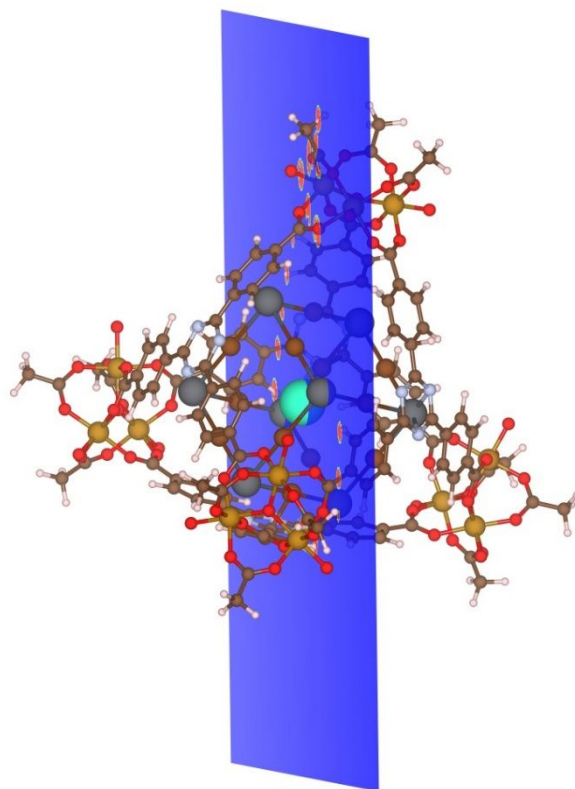
Figure S11. The section of CsPbBr$_3$ QDs in the MOF's cage.
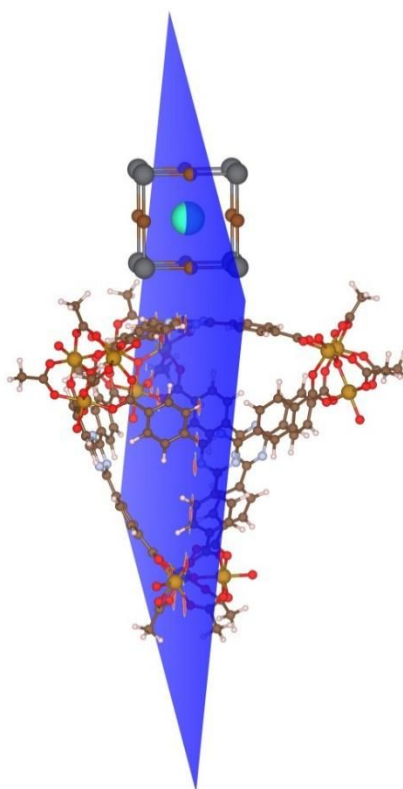
Figure S12. The section of CsPbBr$_3$ QDs outside the MOF's cage.
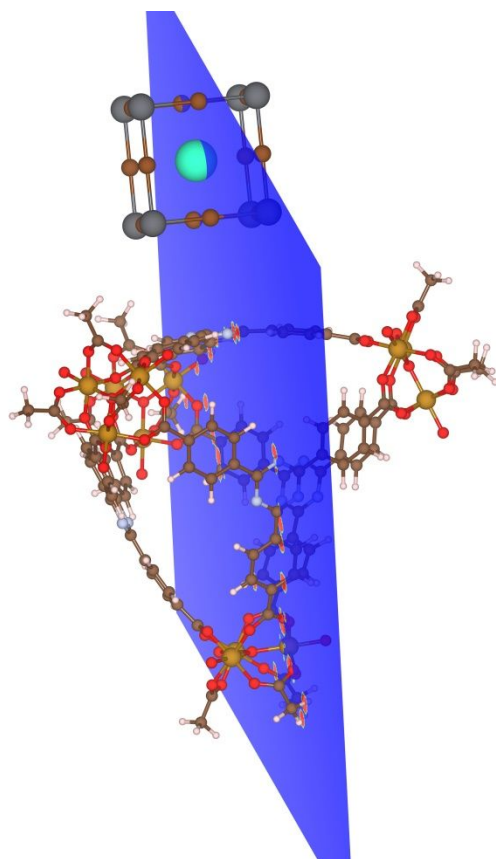
Figure S13. The section of CsPbBr$_3$ QDs far away from the MOF's cage.
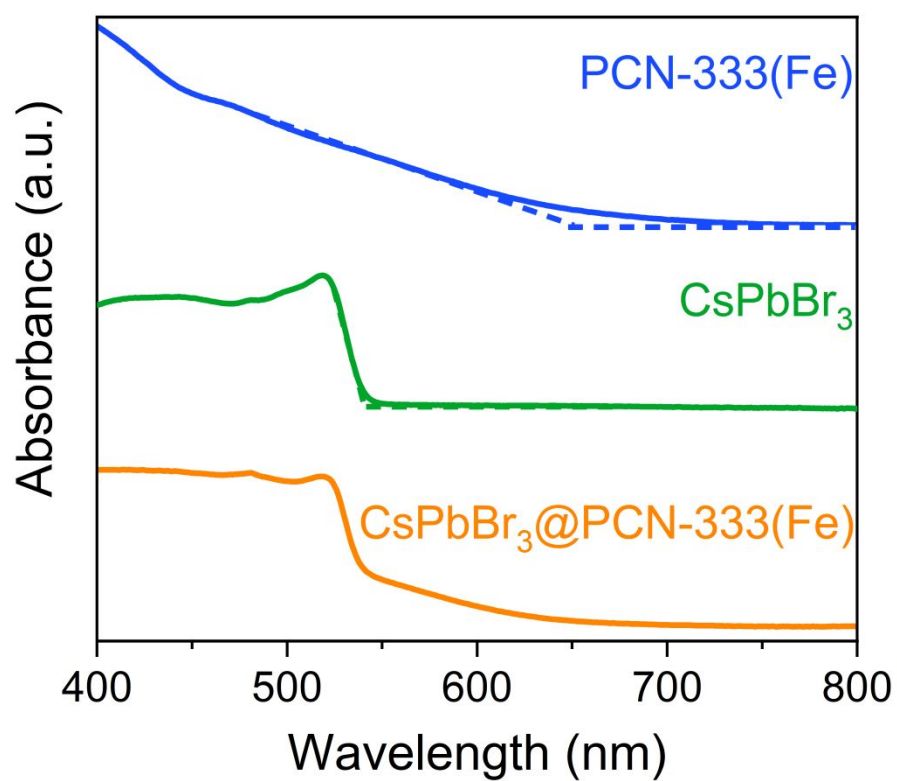
S16. UV–vis Absorption Spectra

Figure S14. UV–vis absorption spectra of CsPbBr$_3$@PCN-333(Fe), PCN-333(Fe), and CsPbBr$_3$ from 400 to 800 nm.
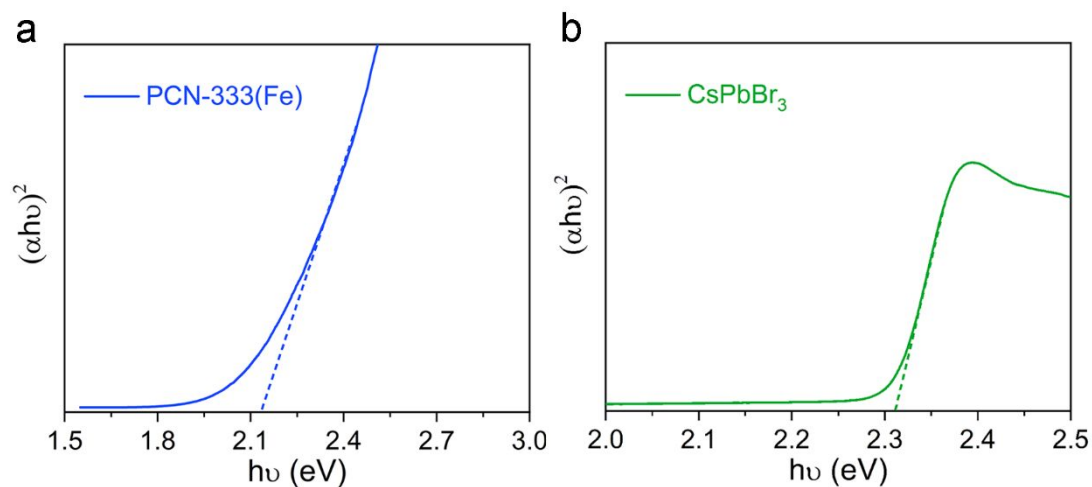
S17. Tauc Plots

Figure S15. Tauc plot of (a) PCN-333(Fe) and (b) CsPbBr$_3$. Estimated band gap of PCN-333(Fe) is 2.13 eV. Estimated band gap of CsPbBr$_3$ is 2.31 eV.

The optical band gap of a semiconductor can be estimated from the Tauc plot which can convert $(\alpha h v)^r$ *versus* hv from the UV–vis spectrum (α, h, and v are the absorption coefficient, Planck constant, and light frequency, respectively; r=2 for a direct band gap material).
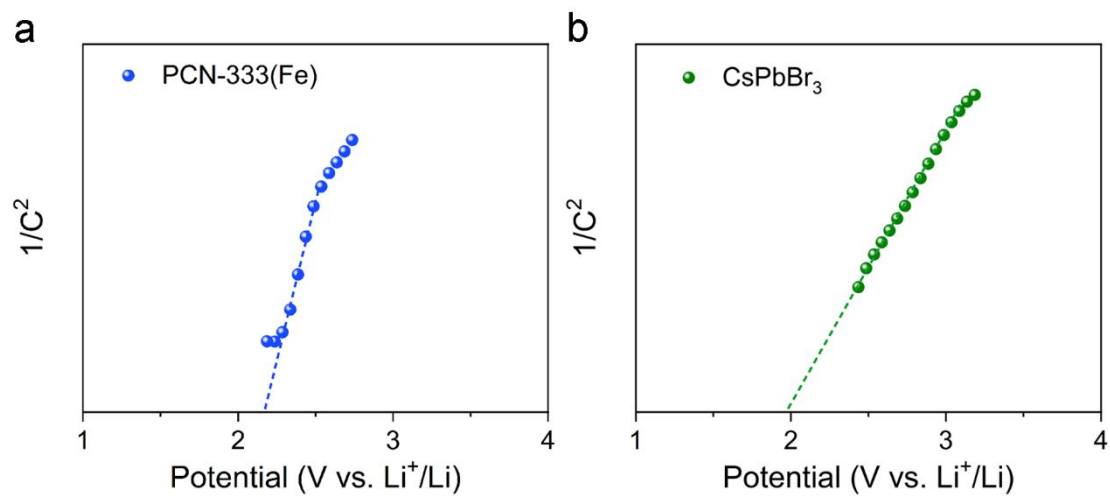
S18. Mott–Schottky Plot

Figure S16. Mott–Schottky plots of (a) PCN-333(Fe), and (b) CsPbBr$_3$.

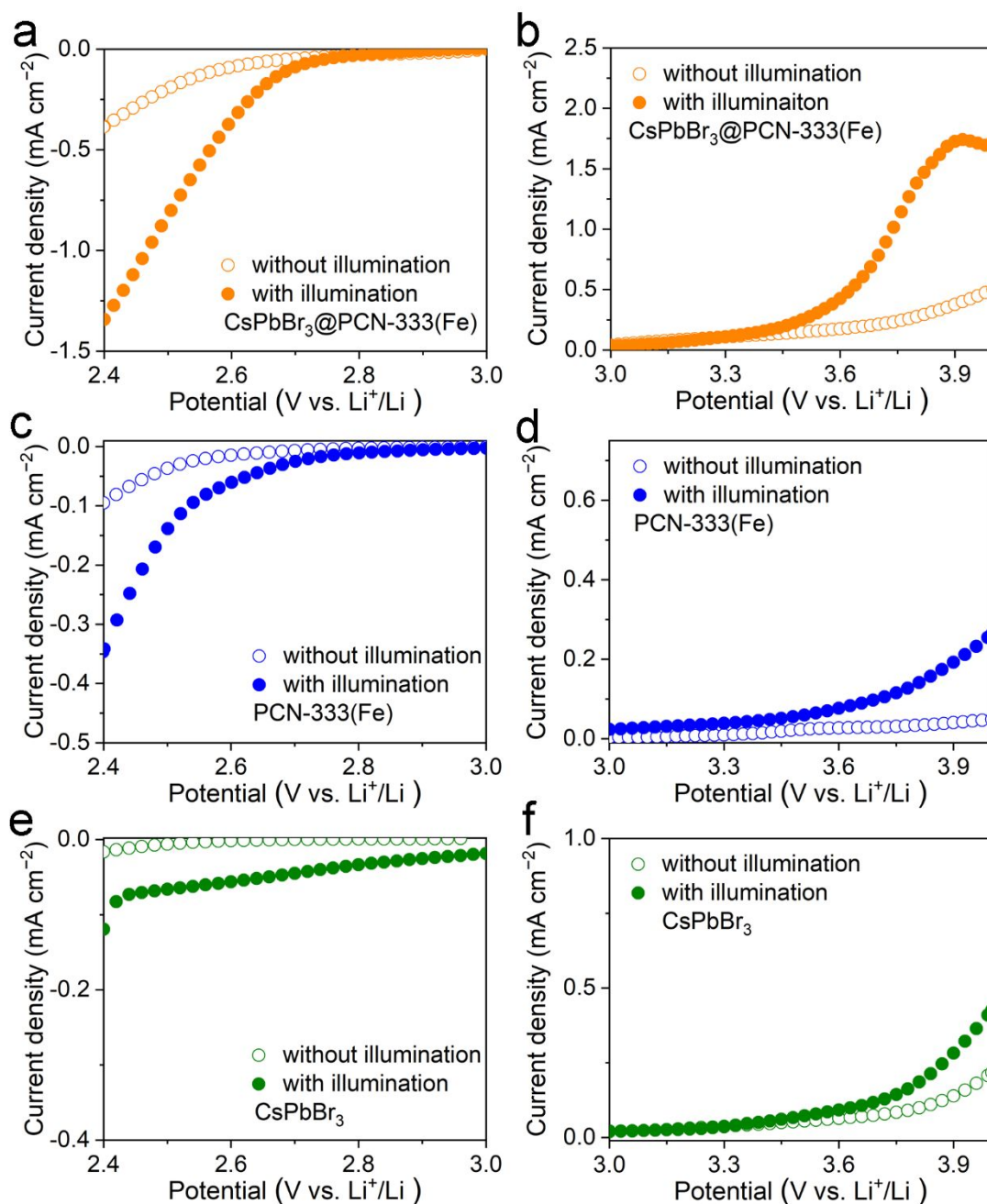## S19. ORR and OER Catalytic Activity with and without Illumination

Figure S17. (a, c, and e) ORR and (b, d, and f) OER catalytic activities of CsPbBr$_3$@PCN-333(Fe), PCN-333(Fe), and CsPbBr$_3$ catalysts in 1 M LiTFSI/TEGDME with and without illumination.
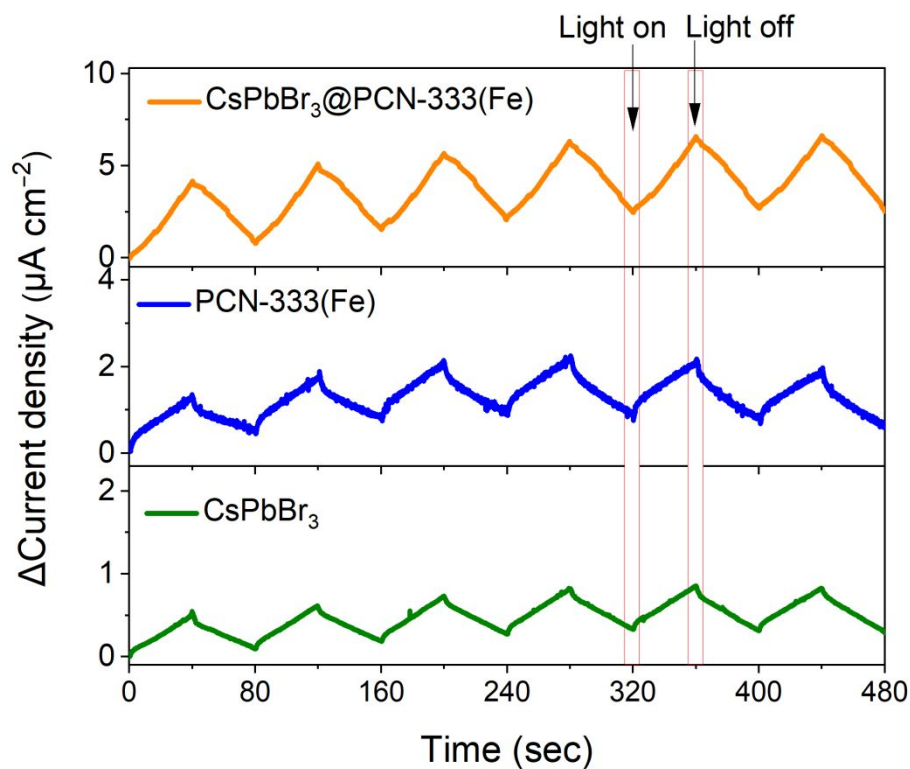
.

S20. Photocurrent Response to Light

Figure S18. Photocurrent response to light for CsPbBr$_3$@PCN-333(Fe), PCN-333(Fe), and CsPbBr$_3$ with an applied bias potential of 0.2 V *versus* open circuit voltage.
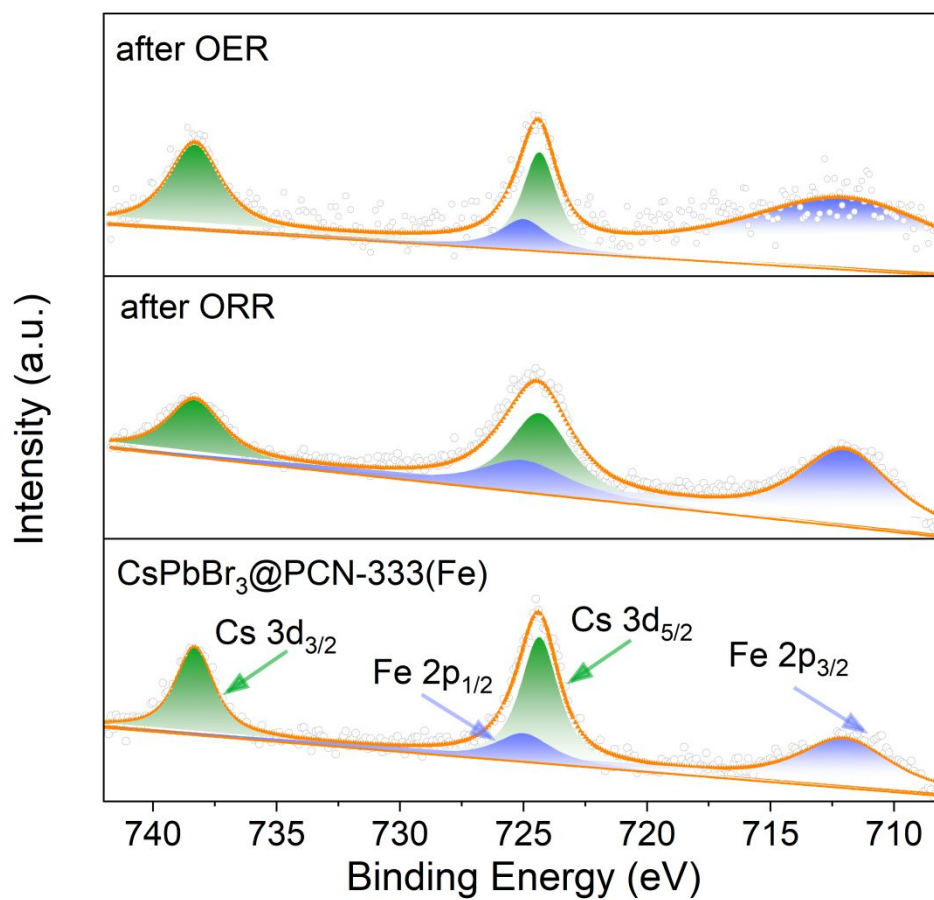
S21. XPS Study after Catalysis

Figure S19. The high-resolution XPS spectra of Cs 3d and Fe 2p for CsPbBr$_3$@PCN-333(Fe) after ORR and OER.
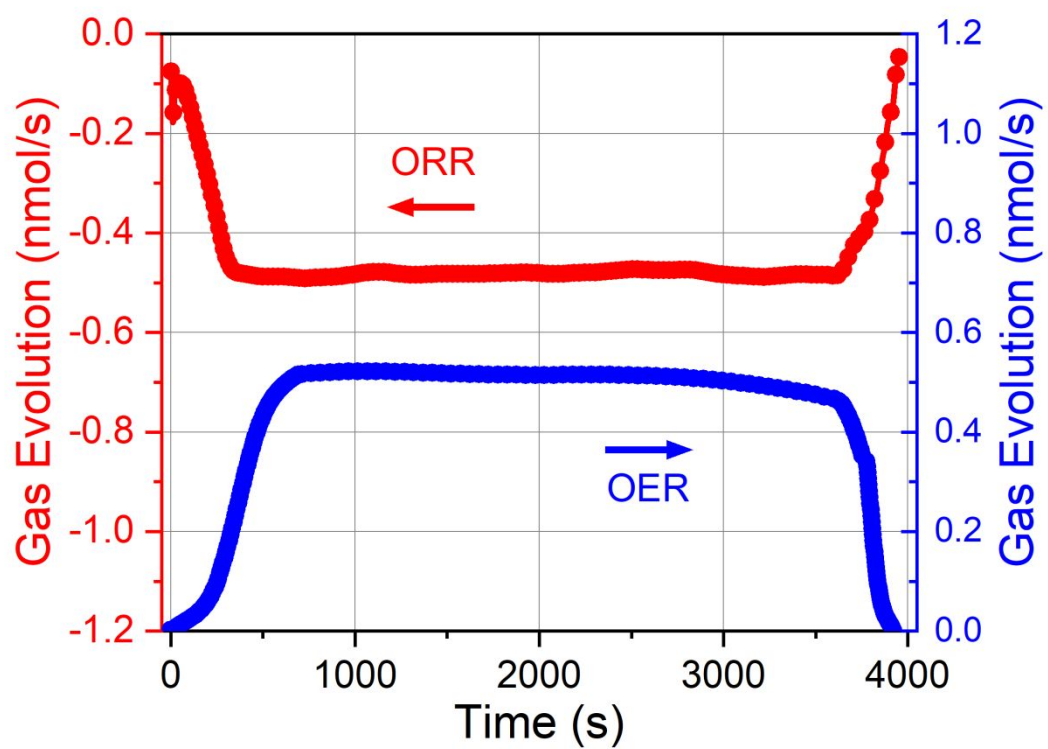
S22. In-itu DEMS Measurements

Figure S20. In-situ DEMS analysis of the gas consumption and evolution during the ORR and OER processes with CsPbBr$_3$@PCN-333(Fe).

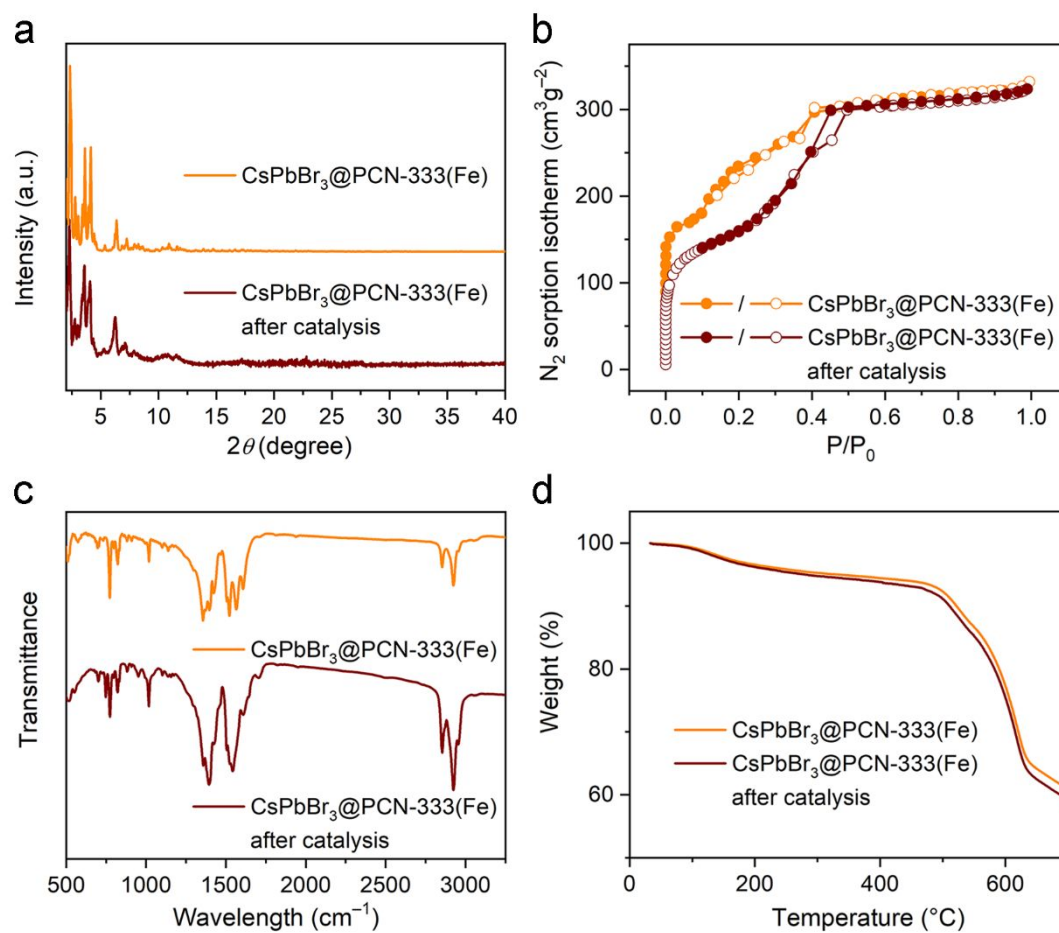## S23. Stability Test of CsPbBr$_3$@PCN-333(Fe) after Catalysis

Figure S21. (a) PXRD patterns, (b) N$_2$ sorption isotherms, (c) IR spectra, and (d) TGA of CsPbBr$_3$@PCN-333(Fe) after catalysis.

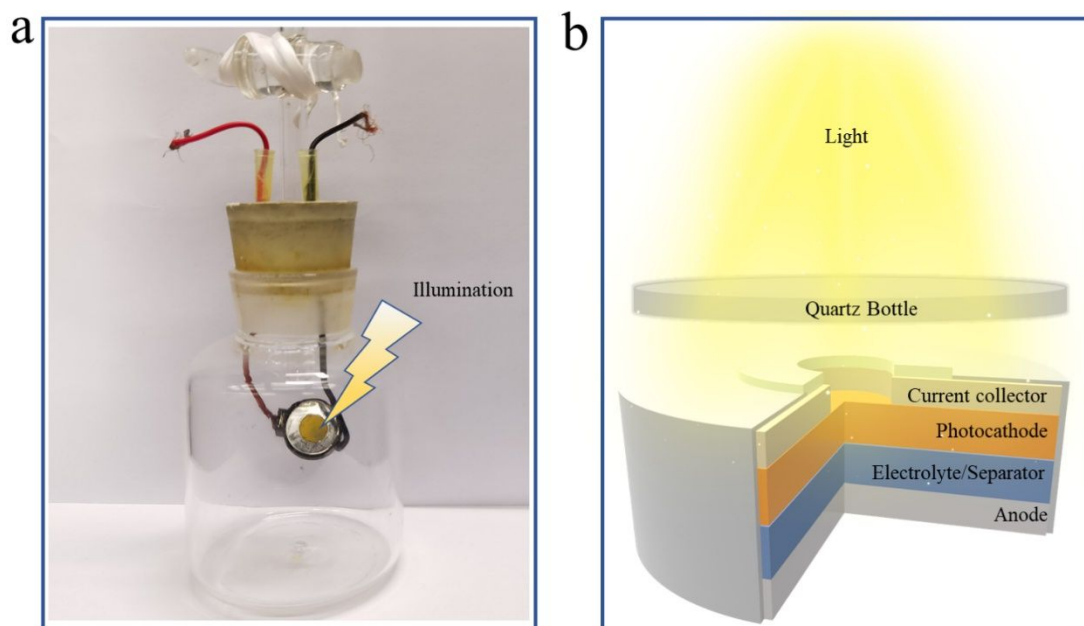## S24. Digital Photo and Schematic Diagram of Light-assisted Li−O₂ Battery

Figure S22. (a) Digital photo of light-assisted Li−O₂ battery test system. (b) Schematic diagram of Li−O₂ battery under light irradiation.

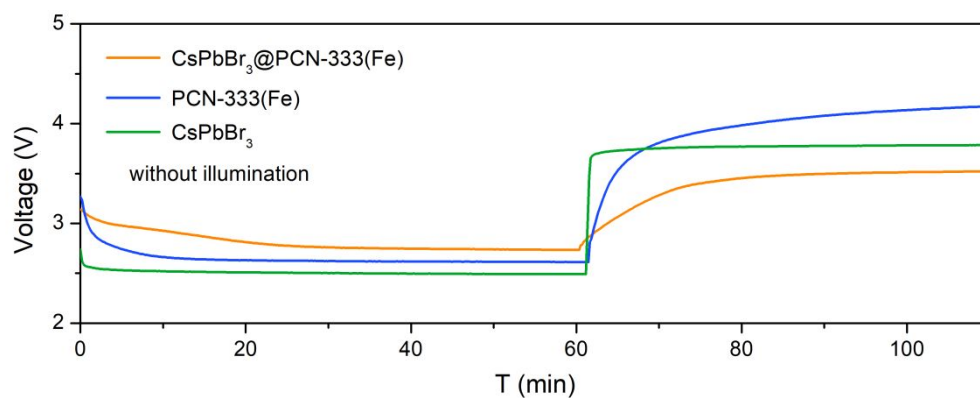## S25. Discharge/Charge without Illumination

Figure S23. Charge and discharge profiles of the batteries with CsPbBr$_3$@PCN-333(Fe), PCN-333(Fe), and CsPbBr$_3$ cathodes at 0.01 mA cm^{-2} without illumination.

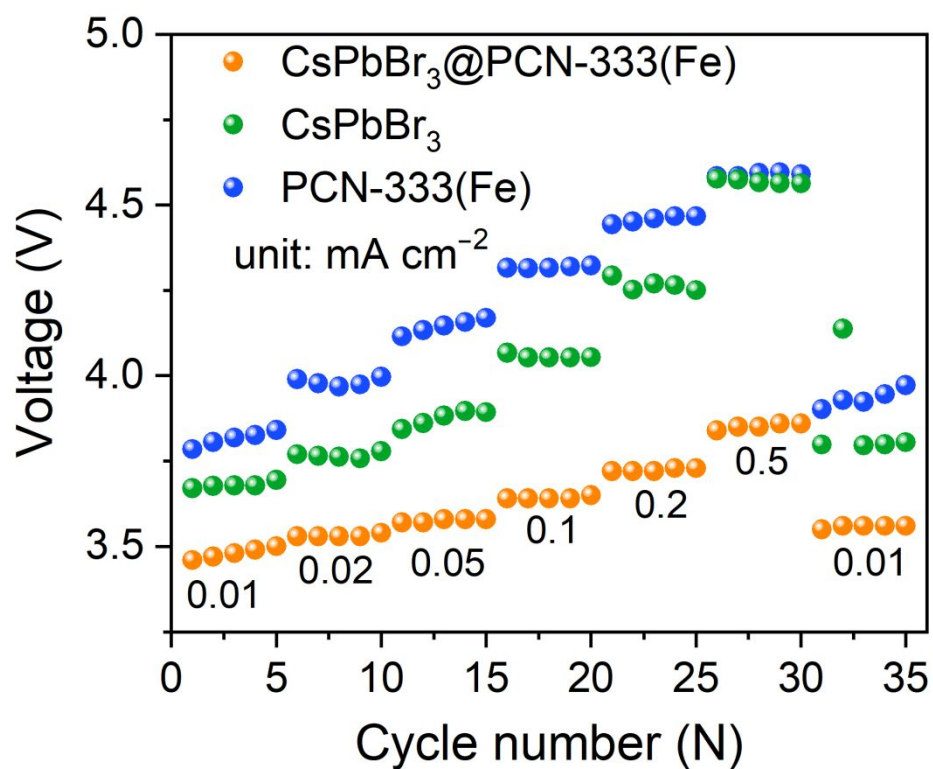## S26. Charge Voltage Variation at Different Current Densities

Figure S24. Charge voltage variation of the batteries with CsPbBr$_3$@PCN-333(Fe), PCN-333(Fe), and CsPbBr$_3$ cathodes at different current densities under illumination.

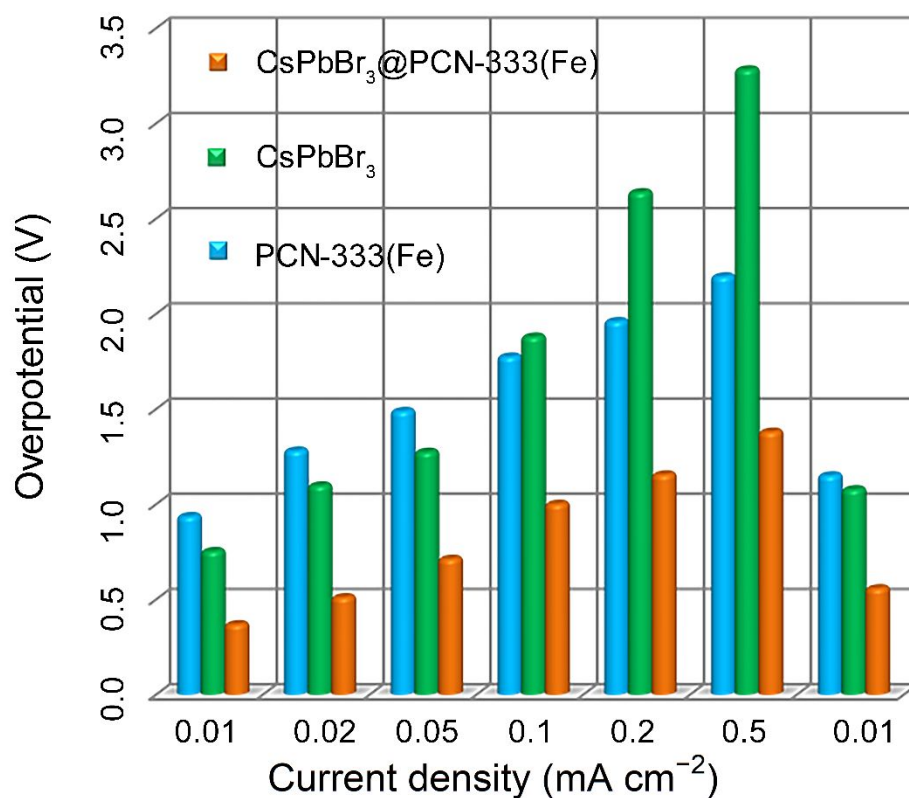## S27. The Average Overpotential of Photo-induced Li–O₂ Batteries

Figure S25. The average overpotential of photo-induced Li–O₂ batteries with CsPbBr₃@PCN-333(Fe), PCN-333(Fe), and CsPbBr₃ as the photo-cathodes at 0.01, 0.02, 0.05, 0.1, 0.2, 0.5, and 0.01 mA cm⁻².

S28. Summary of Onset Potential with CsPbBr₃@PCN-333(Fe), CsPbBr₃, and PCN-333(Fe) for ORR and OER with/without Illumination

Table S1. Summary of the onset potential, overpotential and Δ photovoltage of CsPbBr$_3$@PCN-333(Fe), CsPbBr$_3$, and PCN-333(Fe) for ORR with and without illumination.

Onset potential (V) for ORR			Overpotential (V) for ORR		Δ Photovoltage (V) for ORR
condition	with illumination	without illumination	with illumination	without illumination	difference
CsPbBr$_3$@PCN-333(Fe)	2.65	2.56	0.31	0.4	0.09
CsPbBr$_3$	2.43	2.42	0.53	0.54	0.01
PCN-333(Fe)	2.56	2.54	0.4	0.42	0.02

Table S2. Summary of onset potential, overpotential and Δ photovoltage with CsPbBr$_3$@PCN-333(Fe), CsPbBr$_3$, PCN-333(Fe) for OER with and without illumination.

Onset potential (V) for OER			Overpotential (V) for OER		Δ Photovoltage (V) for OER
condition	with illumination	without illumination	with illumination	without illumination	difference
CsPbBr$_3$@PCN-333(Fe)	3.58	3.77	0.62	0.81	0.19
CsPbBr$_3$	3.72	3.80	0.76	0.84	0.08
PCN-333(Fe)	3.73	3.84	0.77	0.88	0.10

References

1. Kresse, G.; Furthmüller, J., Efficiency of ab-initio Total Energy Calculations for Metals and Semiconductors Using a Plane-Wave Basis Set. *Comput. Mater. Sci*. **1996**, *6*, 15-50.

2. Hammer, B.; Hansen, L.B.; Norskov J.K., Improved Adsorption Energetics within Density-Functional Theory Using Revised Perdew-Burke-Ernzerhof Functionals. *Phys. Rev. B*. **1999**, *59*, 7413-7421.

3. Wang, Q.; Liu, Z.Q.; Liu, D.M.; Wang, W.; Zhao, Z.W.; Cui, F.Y.; Li, G.B., Oxygen Vacancy-Rich Ultrathin Sulfur-Doped Bismuth Oxybromide Nanosheet as a Highly Efficient Visible-Light Responsive Photocatalyst for Environmental Remediation. *Chem. Eng. J.* **2019**, *360*, 838-847.